Journal of Non-Crystalline Solids 624 (2024) 122709

Contents lists available at ScienceDirect

Journal of Non-Crystalline Solids

journal homepage: www.elsevier.com/locate/jnoncrysol

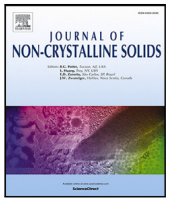

Amorphous matters: Heterogeneity and defects of nanopore silica surfaces enhance CO_2 adsorption

Mattia Turchi [a,*], Sandra Galmarini [b], Ivan Lunati [a]

[a] Laboratory for Computational Engineering, Swiss Federal Laboratories for Materials Science and Technology, Empa, Dübendorf, Switzerland
[b] Laboratory for Building Energy Materials and Components, Swiss Federal Laboratories for Materials Science and Technology, Empa, Dübendorf, Switzerland

ARTICLE INFO

Keywords:
Amorphous surface
Enhanced CO_2 adsorption
Surface defects
Molecular dynamics simulations

ABSTRACT

Despite its importance for many applications (such as catalysis and structure ripening), adsorption on amorphous silica remains poorly understood as most studies focus on crystalline surfaces. Here, we investigate the adsorption of carbon dioxide, CO_2, on hydroxylated silica nanopores by means of molecular dynamics (MD) simulations that compare amorphous and crystalline surfaces. We find that adsorption onto amorphous surfaces is enhanced by the heterogeneity of the structure and by the presence of under-coordinated defects (non-bridging oxygen and threefold coordinated silicon). We identify two classes of adsorption features: (i) a continuous region characterized by an intermediate density of adsorbed CO_2 molecules, which is generated by weak interactions with hydroxyl groups and forms a network that allows molecules to diffuse through the surface adsorption layer; (ii) high-density cage-like features (embedded into the network and induced by the presence of defects) in which CO_2 molecules form multiple short- and long-lived bonds with surrounding atoms and remain adsorbed for a longer time. The rich variety of adsorption features enhances physisorption and leads to longer mean adsorption time than onto the crystalline surfaces. The adsorption time onto amorphous surfaces deviates from the exponential distribution observed in silica crystals and displays a characteristic fat tail. Our findings support the experimental discovery of the potential of defected silica surfaces for CO_2 adsorption and subsequent catalytic conversion to methane, suggesting the possibility of designing and manufacturing specific adsorption features for tailored heterogeneous catalysis.

1. Introduction

Crystalline solids display highly ordered structures that are characterized by a periodic arrangement of atoms and by equal interatomic forces and charge repartition across the chemical bonds of the same type. In contrast, a microscopic periodic structure is absent in amorphous solids, which also lack long-range order. The local variability induced by the disordered state is reflected in non-uniform interatomic forces which may lead, during the manufacturing process, to a much higher concentration of coordination defects on the nanostructured surfaces than what is observed in crystalline solids [1–3].

Non-defected silica structures display a tetrahedral geometry: each silicon atom (Si) is coordinated to four oxygen atoms (Si4) and each oxygen (O) is in turn coordinated to two Si (bridging oxygen, BO). The discontinuity at the surface generates defected sites in the form of under-coordinated silicon (Si3, also referred to as "oxygen vacancies [4]") and oxygen atoms (non-bridging oxygen, NBO). In the presence of water, many of the defected sites are hydroxylated or hydrogenated, and some of the bridging oxygens with strained bonding environment react to form silanol groups [5,6]. At room temperature these processes can occur even at low water partial pressures, leading to a large number of silanol groups at the surface. The amount of persisting coordination defects upon exposure to water also depends on the specific manufacturing process (e.g., colloidal or pyrolytic syntheses) and storing conditions [7,8].

Coordination defects have been observed both experimentally [1,9–11] and in numerical simulations performed by means of density functional theory (DFT) [2,12–15] or molecular dynamics (MD) [16–21]. Walsh et al. performed cluster-based DFT calculations and reported the presence of Si3 and NBO defects (referred to as defect-conserving structures) after surface hydroxylation [22]. The persistence of surface defects is due to the surface roughness which renders some sites inaccessible to water molecules, preventing their hydrogenation or hydroxylation. Mishra et al. [2] observed the presence of Si3 and NBO defects on the amorphous surfaces of dendritic fibrous nanosilica (DNFS) by means of electron paramagnetic resonance (EPR) and further characterized their concentration through X-ray photoelectron

* Corresponding author.
E-mail addresses: mattia.turchi@empa.ch (M. Turchi), ivan.lunati@empa.ch (I. Lunati).

https://doi.org/10.1016/j.jnoncrysol.2023.122709
Received 18 August 2023; Received in revised form 18 October 2023; Accepted 27 October 2023

spectroscopy (XPS). Recent studies [1,2,23] have also reported that surface defects (such as Si3 and NBO) act as catalytic sites in methanation reactions converting carbon dioxide (CO_2) into methane.

The absorption mechanism that occurs on positively charged Si3 sites at amorphous silica surfaces is expected to be somehow similar to the one observed on cations found on crystalline surfaces. In the presence of positively charged surface sites (e.g., transition metals like Fe, Co, Ni, and Cu), the oxygen of the CO_2 forms a bond with the cation and the adsorbed CO_2 molecule assumes an orientation perpendicular to the adsorbent surface [24]. DFT simulations also demonstrated that CO_2 molecules preferentially physisorb between two neighboring silanol, forming bonds with the two hydroxyl groups of hydroxylated crystalline silica surfaces [25].

Even if it is recognized that understanding the role played by surface defects is crucial to master the chemical properties of amorphous silica surfaces [13], the effects of the mutual disposition of defects and of the presence of hydroxyl groups on the adsorption capacities of amorphous substrates have not been investigated. In contrast to MD simulations of physicochemical interactions between fluids and crystals which are fairly common [26–29], numerical studies of the interface between fluids and amorphous solids remain scarce. In part, this is due to the additional challenges that have to be addressed to simulate fluid adsorption onto amorphous surfaces.

First of all, it is necessary to select an adequate combination of force fields to generate the amorphous structures and to model the interaction between the fluid molecules and the surface. Typically, the force fields used in well-established melt-and-quench protocols do not comprise parameters adapted to simulate solid/gas interfaces [30–34]. Therefore, after quenching the amorphous surfaces at ambient conditions, the force fields need to be replaced by more flexible parameterizations that allow the simulation of gas adsorption [26,30,35].

Another challenge is to devise a satisfactory treatment of the partial charges assigned to the surface defects. Due to the surface roughness, it is not possible to hydrogenate or hydroxylate all under-coordinated defects and fractions of Si3 and NBO persist at the surfaces [31]. Although aware of the inherent approximation, several studies reporting the presence of defects on silica/water [21,36] and silica/CO_2 [20] interfaces have employed the same charges for un-defected and defected sites.

Finally, the analysis of the results of the simulations is also a challenge. For instance, the landscape of the adsorption of fluid molecules onto amorphous surfaces is dictated by the heterogeneity of the surfaces and displays very irregular patterns [20]. Irregular adsorption features are not easily amenable to classic tools used to characterize the highly order patterns observed on the crystalline surfaces. New tools and concepts need to be developed to approach adsorption onto amorphous surfaces.

In this work, we investigate the adsorption and the dynamics of CO_2 molecules at hydroxylated defected amorphous silica surfaces with varying defect concentrations. By generating slit nanopores with different amounts of defects and comparing their behavior with similar ordered surfaces, we assess the effects of the physical and chemical heterogeneity (non-symmetrical arrangement of the atoms and presence of defects at the surface, respectively) on the absorption of CO_2. This allows us to discuss the importance and the challenges of dealing with the amorphousness of the substrate.

2. Methodology

2.1. Force fields to generate the nanopores and simulate adsorption

The MD simulations are performed with LAMMPS [37], and employ different force fields to generate the slit nanopores and to simulate CO_2 adsorption at ambient conditions. The defected amorphous nanopores are generated according to a melt-and-quench procedure that follows the well-established method proposed by Du and Cormack [38]. Although melt-and-quench protocols typically employ fixed charges, they have been proven sufficiently accurate in replicating experimentally measured quantities such as glass transition temperature, structural factors (i.e. Si-O bond length, Si–O–Si and O–Si–O angles distributions), percentage of coordination defects and short-membered rings [31,39] (see Table S1 and S2 and Figure S1 in the Supplementary Information). In the melt and quench simulations we employed a force field that comprises only Buckingham and Coulomb terms [38,40], i.e., of the form,

$$E_{ij} = \frac{q_i q_j}{r_{ij}} + A_{ij} e^{-B_{ij} r_{ij}} - \frac{C_{ij}}{r_{ij}^6}, \tag{1}$$

where r_{ij} is the distance between the atoms i and j, q_i and q_j their respective electrical charges, and A_{ij}, B_{ij}, and C_{ij} are the Buckingham parameters (values are given in the Supplementary Information, Table S3).

After generation of the defected surfaces, the Buckingham–Coulomb force field is replaced by ClayFF [35] to describe the nanopores and simulate the hydroxylation of the silica pore as well as the dynamics and surface bonding of the CO_2 molecules, which are described by a flexible version of the EPM2 model [41,42]. For the SiO_2/CO_2 cross interactions terms we employ the parameters optimized and validated by Crabtree et al. [43] and Purton et al. [44]. Both ClayFF and EPM2 are characterized by Lennard-Jones and Coulomb potentials of the form,

$$E_{ij} = \frac{K q_i q_j}{r_{ij}} + 4\varepsilon_{ij}\left[\left(\frac{\sigma_{ij}}{r_{ij}}\right)^{12} - \left(\frac{\sigma_{ij}}{r_{ij}}\right)^{6}\right], \tag{2}$$

where the Lorentz–Berthelot mixing rules are used to obtain the cross terms of the Lennard-Jones parameters, i.e.,

$$\varepsilon_{ij} = \sqrt{\varepsilon_i \varepsilon_j}, \tag{3}$$

and

$$\sigma_{ij} = \frac{\sigma_i + \sigma_j}{2}. \tag{4}$$

All parameters used in the ClayFF and EPM2 FF are reported in the Supplementary Information (Table S4 ans S5), together with a more detailed description of the methodology and a discussion of the bonded terms that describe the silanol group.

Arguably, ClayFF remains one of the best options to model adsorption on amorphous substrates at ambient conditions due to the simple description of pair-wise interactions (i.e., Coulomb and Lennard-Jones) and its applicability to a wide range of chemical species (including specific parameters for silanol surface groups, as well as for Aluminium, Calcium and other alkali and alkaline earth oxides). The applicability of ClayFF has been demonstrated by several works. Bourg et al. [45] showed that ClayFF yields hydroxylated amorphous silica structures which are in agreement with experimental data at room temperature [46,47]. Leroch et al. [30] reported that ClayFF provides an accurate description of humid amorphous silica surfaces and yields water adsorption isotherms for hydroxylated amorphous silica pores which are in good agreement with experimental data [48].

For silica in tetrahedral coordination, ClayFF assigns a partial charge of +2.1 to Si (the formal charge being +4) and of −1.05 to O (the formal charge being -2), hence assuming that a partial charge of ±0.475 is transferred between the oxygen and the silicon in each Si-O bond. Following previous studies [20,21,36], we assign the same partial charges also to under-coordinated Si3 and NBO, potentially leading to an underestimation and overestimation of the defect charge for Si3 and NBO, respectively. To assess the implications of this choice, we also simulated the adsorption on crystal surfaces with modified partial charges (i.e., assigning +2.575 and −1.525 to the Si3 and NBO defects, respectively; a more detailed explanation of the charge variation is provided in the Supplementary Information).

While the modified charges led to slightly more localized adsorption regions, the patterns were comparable to those observed in the surface with unmodified charges and also the conformation of the adsorbed CO_2 molecules was similar (see Figure S2 in Supplementary Information). The effects of the defect charges in the amorphous surfaces are expected to be even smaller than for crystal structure due to the nearby presence of compensating defects (fig. S13).

2.2. Silica pore surface models

We simulate the interaction of CO_2 with the silica surfaces in five slit nanopores formed by slabs of approximate size 100 Å × 100 Å × 19Å and separated by about 20 Å. We generate two crystalline and three amorphous nanopores. For the crystalline pores, we consider a fully hydroxylated crystal pore (FullCr) and a partially hydroxylated crystal pore (PartCr); whereas for the amorphous pores we obtain three structures that differ by their degree of hydroxylation, a high hydroxylation amorphous pore (HighAm), a medium hydroxylation amorphous pore (MedAm), and a low hydroxylation amorphous pore (LowAm).

The crystalline surfaces are generated by cleavage of the Si-O bond normal to the 111 crystallographic plane of β-cristobalite which yields oxygen terminated surfaces (this structure was initially proposed by Puibasset and Pellenq [49] and then extensively used to investigate the interactions of gas and liquid solutions in hydroxylated silica pores [26,28,29,50]). In the FullCr, the oxygen atoms are then hydrogenated leading to two identical surfaces with 4.5 OH/nm^2, which is in the upper range of the reported experimental values [51]. In the PartCr, an equal number of OH groups and H atoms are randomly removed, leaving a surface hydroxyl density of 3.3 OH/nm^2. This creates local coordination defects (Si3 and NBO), generating a local charge imbalance while keeping the overall system charge neutral (a similar approach was used to study aqueous solutions of different electrolytes confined in crystalline silica pores [36]). We remark that the PartCr is a hypothetical crystalline pore that is considered only to isolate the effects of coordination defects and qualitatively understand the impact of local imbalance of electrical charges on the adsorption of CO_2 molecules.

To generate the amorphous-silica slit pores, a 100 Å × 100 Å × 38 Å supercell of β-Cristobalite crystal [52] is melted at 6000 K and quenched at ambient conditions (290 K) according to the protocol detailed in the Supplementary Information. The amorphous structure is then cleaved in the middle to obtain two slabs with an approximate size of 19 Å and a vacuum gap is added to obtain the slit pore. Finally, we create three nanopores with different surface features by annealing the outermost 12.5 Å of each surfaces at three different temperatures (i.e., 1000 K, 1500 K and 2000 K). The resulting annealed surfaces are populated by a different amount of defected sites, which dictates the number of hydroxyls that can be grafted.

As suggested by Du and Cormack [38], we hydroxylate/hydrogenate under-coordinated silicon (Si3) and oxygen atoms (NBO), as well as opened short-membered rings (i.e., two- and three-membered rings, which are closed loops comprising two and three Si atoms, respectively). To locate the short-membered rings at the surface we implement an algorithm based on the definition of Guttman [53]. Once identified, the short-membered rings are opened by breaking a Si-O coordination, which forms vicinal Si3 and NBO sites. Then the surface is equilibrated for 1 ns in the NVT (or canonical) ensemble at 290 K using ClayFF [35]. Finally, the surfaces are hydroxylated by grafting an equal number of OH and H on the Si3 and NBO atoms, respectively [38,40,54], and the hydroxylated pores are equilibrated again at ambient conditions (i.e., for 1 ns at 290 K in the NVT ensemble with ClayFF).

2.3. Simulations of the dynamics of CO_2 in the silica nanopores

Once the slit nanopores are generated, the dynamic of CO_2 molecules is simulated to identify the most adsorptive features and estimate the residence time of the molecules in the surface adsorption layer and in the vicinity of specific adsorption sites. Initially, 100 CO_2 molecules are placed in the center of the slit pores. This number of molecules was used in previous studies [29] and offers a good compromise between effective sampling of the surface and minimization of the CO_2-CO_2 interactions (an analysis of the CO_2-CO_2 coordination number is reported in the Supplementary Information, Figure S4 and S5). All simulations are performed in the NVT ensemble with a time step of 1 fs. Two separated Nosè–Hoover [55,56] thermostats, with a relaxation time of 100 fs, keep the temperatures of the CO_2 and the silica substrate at 290 K. To reduce transient effects, only the last 5 ns of the simulated 10 ns are analyzed (the fluctuations of the thermostat temperatures and the total energy of the system were in the order of ± 5 % after the initial 5 ns, a value that is similar to those reported by previous studies [29,50]). A cutoff of 10 Å is employed for short-range Van der Waals as well as for electrostatic interactions. Long-range Coulombic interactions are treated by the staggered 3Particle–Mesh (PPPM) method [57–59] with an accuracy of 10^{-4} .

2.4. Determination of the cutoff defining the adsorbed CO_2 molecules

To analyze the adsorption time, we define the position of the CO_2 molecule as the position of the carbon atom. The molecule is considered adsorbed at the interface layer as long as the distance of the carbon atom from the surface is smaller than a cutoff value, which is defined from the excess of CO_2 density in the profiles perpendicular to the pore surface (Figure S6 in the Supplementary Information). We also consider the residence time and adsorption onto specific surface sites. In this case, the molecule is considered adsorbed as long as it remains within a spherical region centered on the specific site. The cutoff that defines the spherical adsorption region is selected from the radial distribution function (RDF) between the surface site and the CO_2 molecule (Figure S9 and S10 in the Supplementary Information).

The pore surfaces are characterized by the presence of hydroxyl (OH), tetrahedrally coordinated silicon (Si4), under-coordinated silicon (Si3), fully coordinated bridging oxygen (BO), and under-coordinated non-bridging oxygen (NBO). The coordination of oxygen and silicon atoms is inferred from the Si-O RDF (Figure S7 and S8 in the Supplementary Information), which suggests that a distance of 2.4 Å is the upper limit to consider a Silicon/Oxygen pair as coordinated and can be used to differentiate Si4 from Si3 and BO from NBO. As the RDF analysis between the sites and the CO_2 molecules shows no CO_2-density excess close to Si4 and BO, we consider only Si3, NBO, and OH groups as adsorptive sites. To define the spherical adsorption regions we use $r_{Si3,NBO}$ = 4.5 Å and r_{OH} = 5.5 Å. This combination of cutoff values was capable of encompassing the majority of CO_2 molecules adsorbed in the surface layer. (For a detailed discussion about the spherical cutoffs see the Supplementary Information, as well as Figure S11, Tables S6 and S7).

2.5. Time correlation analysis

To perform the time correlation analysis we track the evolution of the molecules that are found within a certain region at an initial time, and we determine the distribution of their residence time. From the initial time frame, we count the number of CO_2 molecules, $N(t_0)$, that are contained in the volume delimited by the cutoff (i.e., the cutoff defining the surface layer or the spherical cutoff defining the neighborhood of the specific sites). From any successive frame at time t, we count the number of molecules that are still found in the same region, $N(t)$, whereas the other molecules are considered to be desorbed. We consider different initial time frames and track the presence of CO_2

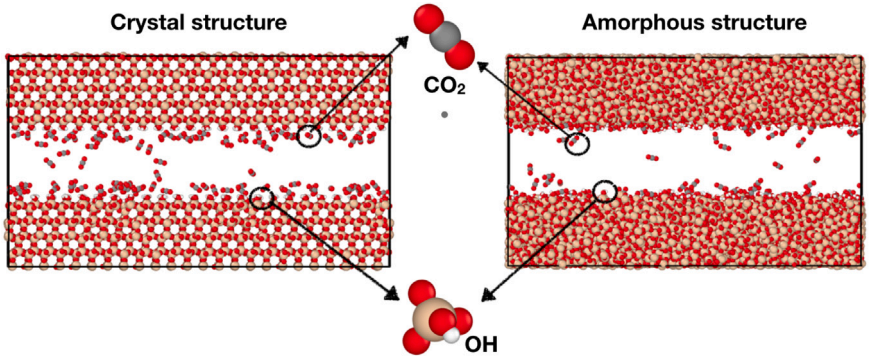

Fig. 1. Snapshot of the simulations of the dynamics of CO_2 molecules in crystalline (left) and amorphous (right) slit nanopores. Silicon, oxygen, hydrogen and carbon atoms are reported in gold, red, white, and gray, respectively. The system consists of a pore of a width of 2 nm that contains 100 CO_2 molecules.

molecules in the adsorption regions in time windows of 400 ps, which are discretized into 200 time frames with a uniform time difference of 2 ps. To increase the statistics of the adsorption events, a total of 70 time windows are considered over the final 5 ns of the simulation.

The residence times (or desorption times) obtained from all time windows are plotted together and fitted to an exponential or to a double-exponential function of the form,

$$\frac{N(t)}{N(t_0)} = a\exp\left(-\frac{t}{\tau_1}\right) + (1-a)\exp\left(-\frac{t}{\tau_2}\right). \quad (5)$$

The fitting allows us to identify the mean residence times (τ_1 and τ_2) and the fraction of CO_2 molecules, a, with mean residence time τ_1. First, a fit to a single exponential function (i.e., $a = 1$) is attempted; if the data are not satisfactorily described by a simple exponential, they are fitted to a double-exponential function (Eq. (5)). If the error on the second time constant is smaller than its value, the double exponential is used, otherwise data are still fitted to a single exponential. The error on the parameters is estimated calculating the standard deviation from the covariance matrix, hence, taking the square root of the corresponding variance (i.e., the diagonal term). We remark that even if we found that the double exponential approximates well the residence-time data, this does not necessarily imply that only two types of adsorption sites are relevant to describe the behavior of the surface, and other distributions and decay models could be considered.

3. Results and discussion

3.1. Characterization of the slit-pore surfaces

The surfaces of the five pores are characterized by the surface roughness, as well as by different number densities of the OH, Si3, and NBO sites that remain after hydroxylation/hydrogenation. Whereas the characterization of the crystal surfaces is rather straightforward thanks to their regular periodic structure, amorphous surfaces display a pronounced heterogeneity. The different surface features dictate the adsorption of CO_2 and need to be carefully characterized (Fig. 1).

To characterize the roughness of the surface, we consider the width of the peaks of the OH-density at the pore surfaces and the width of the transition regions to the bulk Si-density. Both widths are estimated around 5–6 Å for all the amorphous substrates, independently of the annealing temperature used in the melt-and-quench protocol (Figure S12 in Supplementary Information). In contrast, the number of coordination defects and OH groups at the surface depends on the annealing temperature employed in the melt-and-quench simulations [51,60]. The number of dangling bonds decreases when the annealing temperature increases, in agreement with experimental observations obtained from electrical-conductivity measurements [61,62]. After hydroxylation/hydrogenation, the surface densities of hydroxyl groups are 1.8 OH/nm^2, 2.3 OH/nm^2, and 2.5 OH/nm^2 on the surfaces annealed at temperature 2000 K (LowAm), 1500 K (MedAm), and 1000 K (HighAm), respectively (Table 1). These values are in the experimental range reported by Zhuravlev et al. [51,60], and lower than those observed on the crystalline surfaces (i.e., 4.5 OH/nm^2 and 3.3 OH/nm^2 on the FullCr and PartCr, respectively).

A fraction of Si3 and NBO persisted at the surfaces after hydroxylation/hydrogenation because they could not be grafted due to geometric hindrance induced by the surface roughness. The Si3/OH and NBO/OH ratios observed in the three amorphous pores (Table 1) are in same order of the values reported by Fogarty et al. [17] (i.e., Si3/OH = 0.11 and NBO/OH = 0.04) who used MD simulations with the reactive force field ReaxFF to study amorphous silica surfaces in water. The defects/OH ratios are lower than those experimentally measured on the amorphous surfaces of dendritic fibrous nanosilica (DNFS) by Mishra et al. [2] (values are reported in the Supplementary Information).

In contrast to the surface density of hydroxyl groups, the densities of Si3 and NBO sites that remain after hydroxylation do not display a clear trend with the surface annealing temperatures (Table 1). The MedAm displays Si3/OH and NBO/OH ratios of 0.05 and 0.04, respectively, which are not only lower than in the HighAm (Si3/OH = 0.10, NBO/OH = 0.09) but also lower than in the LowAm (Si3/OH = 0.08, NBO/OH = 0.07), even if more coordination defects are observed in MedAm than in LowAm after melt and quench (Table S1 in Supplementary Information). Although this could be in part due to statistical fluctuations, it is possible that an annealing temperature of 1500 K yields less stable Si3 and NBO defects, which are more likely to recombine during equilibration. Indeed, the MedAm displays a higher recombination rate during the equilibration that follows the breakage of the short-membered rings. This is also consistent with the observation that MedAm has the highest proportion of vicinal Si3–NBO pairs (almost 90% of the charge of the Si3 is compensated by a NBO at less than 4 Å, in contrast to around 55% for the HighAm and 80% for the LowAm; see Figure S13 in the Supplementary information).

The cumulative RDFs of the defect distribution show that the majority of Si3–NBO pairs on the amorphous surfaces can be found at a distance between 3 and 4 Å (Figure S13 in the Supplementary Information), which corresponds to the location of the vicinal Si-O peak in the Si-O RDFs (Figure S8 in the Supplementary Information) and is consistent with the presence of vicinal silanols that has been experimentally observed [51]. On the crystalline surface, whose cleavage plane has been chosen to obtain a silanol density in the experimental range, the adjacent dangling Oxygens are at a distance of around 5 Å. They are bonded to the next-nearest Si atoms and there are no vicinal Si3/NBO defect pairs possible on this surface. Even when a neighboring pair of OH^- and H^+ is removed, the resulting Si3 and NBO are at a larger distance than the vicinals found in the amorphous pores, leading to a typical distance between Si3 and NBO of 4 to 6 Å (Figure S13 in Supplementary Information). On the amorphous surfaces, Si3, NBO, and OH are closer to each other than in PartCr and are arranged in a non-symmetric manner. This is expected to have a major impact on the adsorption behavior.

Table 1
Number of OH, Si3 and NBO sites, together with Si3/OH and NBO/OH ratios for the five different pores and the values inferred from the work of Fogarty et al. [17].

	T[a]	OH/nm^2	Si3/nm^2	NBO/nm^2	Si3/OH	NBO/OH
FullCr	NA	4.5	0	0	0.00	0.00
PartCr	NA	3.3	0.8	0.8	0.23	0.23
LowAm	2000 K	1.8	0.15	0.13	0.08	0.07
MedAm	1500 K	2.3	0.10	0.09	0.05	0.04
HighAm	1000 K	2.5	0.25	0.24	0.10	0.09
ReaxFF [17]	4000 K	5.4	0.66	0.24	0.12	0.04

Table 2
Parameters of the functions fitted to the residence time data for the surface layer.

	FullCr	PartCr	LowAm	MedAm	HighAm
τ_1 (ps)	26 (3)	17964 (27428)*	39 (15)	32 (14)	54 (24)
τ_2 (ps)	–	–	129 (55)	92 (58)	203 (78)
a	1	1	0.60 (0.30)	0.67 (0.42)	0.51 (0.27)

The functions considered are of the form $N(t)/N_0 = a\exp(-t/\tau_1) + (1-a)\exp(-t/\tau_2)$, where N_0 is the number of molecules that are initially adsorbed, $N(t)$ the number of molecules that are still adsorbed at time t, τ_1 and τ_2 the mean adsorption times, and a the relative importance of the time constant τ_1. For the crystal pores (FullCr and PartCr) a simple exponential is fitted to the data ($a = 1$); whereas a double-exponential function is required for the amorphous pores. The uncertainties on the fitted parameters, estimated as the standard deviation obtained from the covariance matrix, are given in parenthesis.
* Notice that residence time of the PartCr is significantly longer than the time window used for the analysis (400 ps), hence, the analysis is very approximate.

3.2. Residence time at the surface adsorption layer

To investigate the interaction of CO_2 molecules with the nanopore surface and understand the impact of different features (e.g., OH, Si3 and NBO) on the adsorption, we perform a time correlation analysis to determine the distribution of the adsorption time of CO_2 molecules. The desorption curves (fraction of molecules still adsorbed at time t) are plotted in Fig. 2 along with the exponential (FullCr) or double-exponential (HighAm, MadAm, LowAm) fits. The mean residence times and their relative importance are given in Table 2.

In FullCr, the desorption of CO_2 molecules from the surface layer is well described by a single exponential decay with a mean residence time of 26 ps (Fig. 2a), which agrees with results reported by Le et al. [29] for the same system (i.e., CO_2 within a β-cristobalite pore of 2 nm of width). This behavior is due to the homogeneity of the pore surface which is characterized by OH groups arranged on a hexagonal regular lattice: each adsorbed molecule experiences the same interaction with the hydroxyl and has the same probability to desorb. In the PartCr, the residence time of the CO_2 molecules at the surface layer is much longer than the size of the time window used for the time correlation analysis (400 ps) and cannot be accurately estimated (the standard deviation of the mean residence time is very large; Table 2). Even if it cannot be accurately determined, the mean residence time of the adsorbed CO_2 at the PartCr surface is clearly much longer than in the other pores (the decay profile for the PartCr is reported in Figure S2 of the Supplementary Information).

The desorption of the CO_2 molecules from the surface layer of the amorphous pores does not follow a simple exponential and a double-exponential function is employed to describe the decay of the number of adsorbed molecules (Fig. 2 b,c,d). For all amorphous surfaces, the fitted parameters indicate a short mean residence time τ_1 in the range between 32 ps and 54 ps, and a long residence time τ_2 in the order of 92 ps to 203 ps. Although the differences between the predicted mean residence times are within the parameters uncertainties estimated by the standard deviation, there is a consistent trend for the surfaces with a higher concentration of defects (i.e., with more Si3 and NBO sites, hence, in order HighAm → LowAm → MedAm — see Table 1) to exhibit a longer residence time (i.e., larger τ_1 and τ_2 and a smaller fraction, a, of molecules desorbing with the shorter mean residence time), suggesting that the coordination defects have direct impact on the bonding of the CO_2 molecules. Notice also that, in the amorphous pores, τ_1 is always larger than the mean residence time observed in the FullCr, whereas τ_2 is much smaller than the residence time of PartCr. This is due to the heterogeneity of the local chemical environment of the adsorption sites on the amorphous surfaces, as well as their non-symmetrical arrangement, which results in a different interaction between the CO_2 molecules and each adsorption site.

3.3. Relationship between CO_2 adsorption and the local structure of the surface

To understand the characteristics that dictate adsorption at the surface of the nanopores, we calculate the (time-averaged) surface density of adsorbed CO_2 molecules and plot the surface-density maps for the crystalline and amorphous nanopores in Figs. 3 and 4, respectively (only one of the two surfaces is shown for each pore).

On the FullCr surface, the CO_2 molecules form a continuous intermediate-density (0.75–2.5 CO_2/nm^2) pattern with a honeycomb structure (Fig. 3a). This results from the symmetric arrangement of the underlying OH groups, which characterizes the fully hydroxylated crystal surface. In fact, the intermediate-density regions are located between two OH groups, indicating that bonds are formed with two hydroxyls (see Fig. 3a and Figure S2 in the Supplementary Information), as also reported by other studies [29,63]. On the surface of PartCr, high CO_2 densities are confined at specific locations, which correspond to CO_2 molecules that are adsorbed on top of the Si3 sites. Overall, the density maps of the two crystalline surfaces are clearly distinct: on the FullCr surface the intermediate-density region forms a connected network with a honeycomb structure, whereas the PartCr surface exhibits clearly separated islands of very high density (three orders of magnitude higher than in the FullCr).

The CO_2 density distributions on the amorphous surfaces exhibit features that remember both the FullCr and the PartCr: a network of intermediate density coexists with high-density adsorption islands. The network is reminiscent of the connected honeycomb lattice of the FullCr and displays rather similar CO_2 densities. However, the network is distorted and less clearly connected due to the disordered distribution of the OH groups on the amorphous surfaces (Fig. 4). Similarly, the high-density islands on the amorphous surfaces are reminiscent of the high-density spots observed on the PartCr, but they become stretched and irregular, loosing the approximately circular shape observed on the PartCr surface and displaying a maximum density which is one order of magnitude smaller (similar patterns have been reported by Yang et al. [20] who investigated the adsorption of dense CO_2 on fully dehydroxylated amorphous silica surfaces characterized by a high density of coordination defects). In contrast to the PartCr surface (where the high-density spots are clearly associated to Si3 defects, see Fig. 5a), most of the high-density regions on the amorphous surfaces are associated to multiple surface groups. Although coordination defects still play a primary role, the CO_2 molecule simultaneously interacts with multiple adsorption sites and species (see Fig. 5 b, c, d).

3.4. Residence time for specific adsorption sites (OH, Si3 and NBO)

To understand the impact of the specific adsorption sites on the sorption dynamics, we analyze the residence time of the CO_2 in the spherical neighborhood of the OH, Si3 and NBO sites. Even if on the amorphous surfaces the actual adsorption regions are irregular and elongated (Fig. 4), the bonding with a specific site requires the distance to be smaller than a certain value that can, as a first approximation, be described by the spherical cutoff.

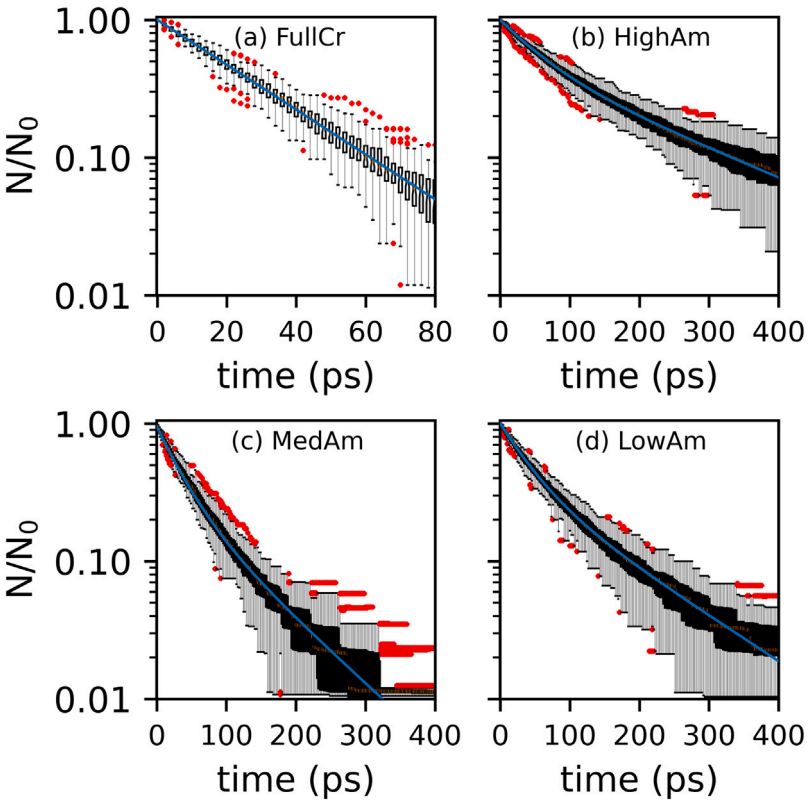

Fig. 2. Fraction N/N_0 of the initially adsorbed CO_2 molecules still adsorbed at the surface layer after time t. Results for (a) the fully hydroxylated crystal pore (FullCr), (b) the high hydroxylation amorphous pore (HighAm), (c) the medium hydroxylation amorphous pore (MedAm), (d) the low hydroxylation amorphous pore (LowAm). The box plots represent the 0.25–0.5 quartiles (with whiskers extending for 1.5 times the inner quartile range), whereas the red dots are data outliers. The blue line is the fitted exponential (for the FullCr) or double-exponential functions (for the other three pores) with parameters given in Table 2.

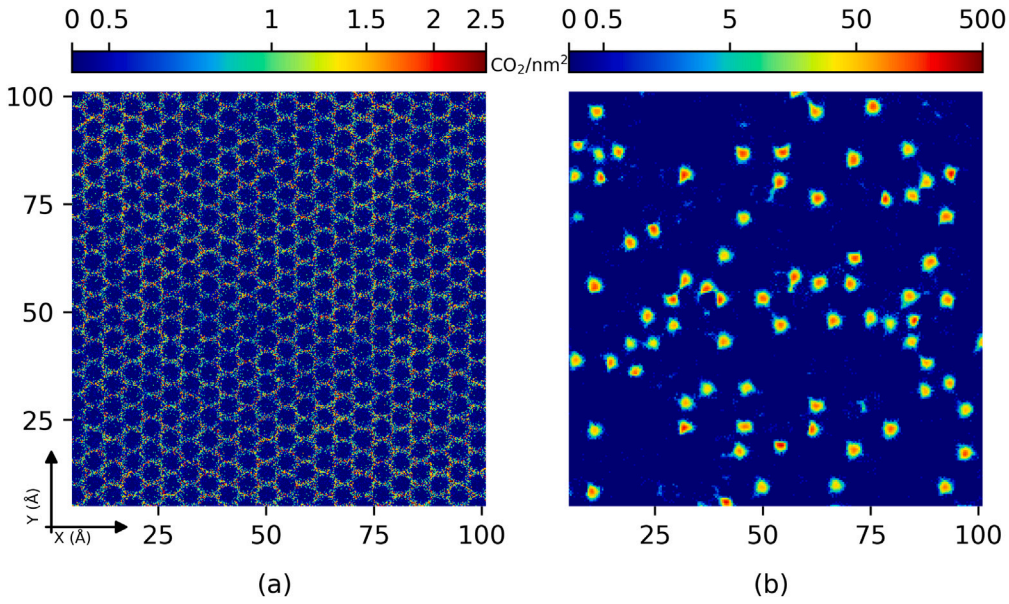

Fig. 3. Spatial distribution of the time-averaged number density of CO_2 molecules adsorbed at the crystalline pore surfaces: (a) FullCr, (b) PartCr. The surface density is computed by subdividing the xy plane into 500 × 500 bins. The number of CO_2 molecules in each frame is averaged over the last 5 ns of the simulation (which corresponds to 5000 frames) and normalized by the area of the bins. Only one of the two pore surfaces of the slit pores is shown. CO_2 molecules are considered adsorbed if they are within the surface cutoffs selected for the interface layer in question.

We consider two hypotheses: (i) the adsorption results from a stable simultaneous bonding with multiple-sites, such that the molecule is considered desorbed as soon as it leaves the intersection of the spherical neighborhoods; (ii) the adsorption is dominated by one of the adsorption sites (only weaker and short-lived secondary bonds are formed with the other sites), hence, the molecule is considered desorbed when it leaves the spherical neighborhood of the dominant site (in other words, a molecule that leaves the intersection region is still adsorbed if it remains within the cutoff distance from the dominant site). In general, the multiple-sites bond analysis (first hypothesis) leads

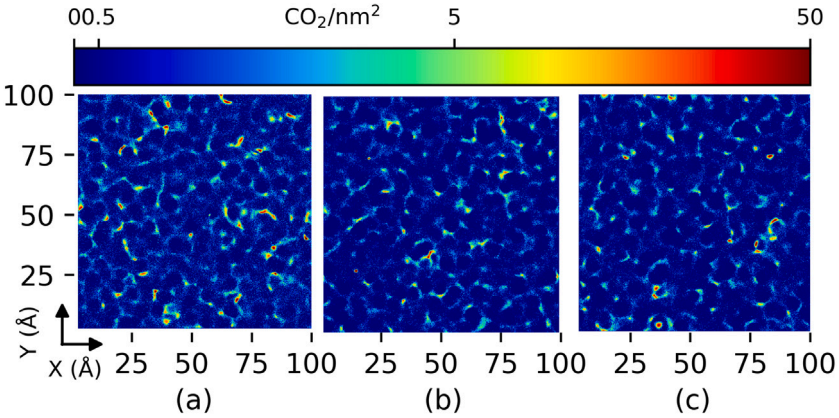

Fig. 4. Spatial distribution of the time-averaged number density of CO_2 molecules adsorbed at the amorphous pore surfaces: (a) HighAm, (b) MedAm and (c) LowAm. The surface density is computed by subdividing the xy plane into 500 × 500 bins. The number of CO_2 molecules in each frame is averaged over the last 5 ns of the simulation (which corresponds to 5000 frames) and normalized by the area of the bins. Only one of the two pore surfaces of the slit pores is shown. CO_2 molecules are considered adsorbed if they are within the surface cutoffs selected for the interface layer in question (Figure S6 in Supplementary Information).

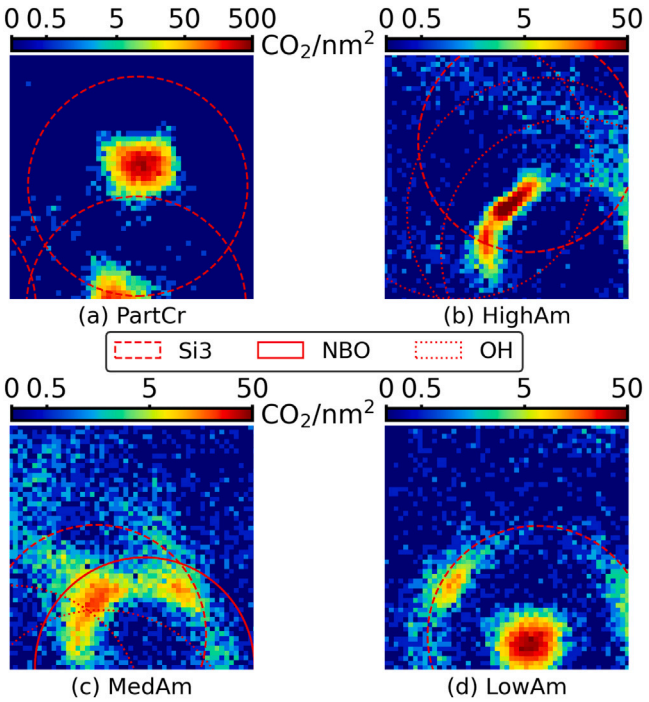

Fig. 5. Detail of the CO_2 density distribution in regions of size 10 Å × 10 Å containing the adsorption sites (Si3, NBO and OH): (a) in the PartCr high-density of CO_2 molecules is typically located at the center of the circle representing the cutoff distance from an isolated Si3; (b) a high-density region generated by the adsorption in a cage structure formed by a Si3 and three OH in the HighAm; (c) a cage structure formed by Si3, NBO, and two OH in the MedAm; (d) a high-density region generated by an isolated Si3 site in the LowAm. The circles represent the projection on the xy-plane of the spherical regions centered on the Si3, NBO and oxygen atoms of the OH. The radii are calculated according to the spherical cutoffs of each defect and group.

to short residence times with little difference between the different bonding environments (the results are reported in Table S7 of the Supplementary Information). Even if it is reasonable to assume that multiple sites simultaneously participate to the adsorption, the intersection regions are too small and inapt to describe the irregular shapes of the high-density regions. Therefore, we discuss only the results of the dominant-bond analysis (second hypothesis), assuming that the other involved sites only contribute with secondary short-lived bonds.

3.4.1. Crystalline pores

In the FullCr, only OH groups adsorb the CO_2 molecules, which preferentially form an angle of about 50 deg with respect to the normal to the surface. The carbon atom is located in between two OH groups (Supplementary Information, Figure S14), in agreement with what reported by Le et al. [29]. Due to the periodic structure of the crystal, all OH groups are identical and only thermal agitation may introduce small variations in the inter-atomic distance. This homogeneity is reflected by the statistics of the adsorption time: the decaying of the number of CO_2 molecules that are adsorbed in the spherical neighborhoods of the OH groups is well described by a single exponential function. This is the signature of adsorption bonds that are similar and adsorbed molecules that have approximately the same probability to desorb, regardless to the specific OH group to which they are bound. The mean adsorption time estimated by exponential fitting of the residence-time data is τ_1 = 8 ps (Table 3), which is less than a third of the mean residence time in the surface layer, i.e., τ_1 = 26 ps (2). This discrepancy is due to the fact that the CO_2 molecules diffuse through the honeycomb structure formed by the OH groups, moving from one adsorption region to the other, before being desorbed from the surface layer. CO_2 molecules that diffuse at the pore surface by moving between adjacent adsorption sites have been observed in the simulations.

In the PartCr, the adsorption is dominated by the Si3 sites that adsorb about 95 of the 100 CO_2 molecules and exhibit a mean adsorption time of about 1500 ps (Table 3). The CO_2 molecules adsorbed on Si3 sites are orientated perpendicularly to the surface, and the closer oxygen forms a van der Waals bond with the positively charged Si3 (Figure S14 in the Supplementary Information), in analogy to CO_2 molecules adsorbed onto transition metal cations [24]. Only a few molecules are adsorbed by OH and NBO (i.e., 2.4 and 1.9 out of 100 CO_2 molecules, respectively). Although the mean adsorption time is smaller than for the Si3 (Table 3), it is substantially larger than for the OH on the FullCr surface. This longer mean residence time is due to the proximity of Si3 sites, which affect also the residence time in the spherical neighborhood of the OH.

3.4.2. Amorphous pores

In the amorphous pores, the OH groups adsorb a significantly larger number of CO_2 molecules than the NBO and Si3 (Table 3). This is due to the higher surface density of OH groups with respect to NBO and Si3 groups (Table 1). The Si3 are clearly less dominant than in the PartCr, where the Si3 adsorb almost all molecules. Moreover, while the NBO sites play a negligible role in the PartCr, on the amorphous surfaces we observe more bonding to NBO than to Si3. There are two possible reasons for the reduced importance and strength of adsorption of the

Table 3
Parameters of the functions fitted to the residence time data for each specific adsorption site (i.e., OH, Si3, and NBO).

	Parameter	FullCr	PartCr	LowAm	MedAm	HighAm
OH	τ_1 (ps)	8 (1)	269 (16)	7 (1)	8 (1)	10 (2)
	τ_2 (ps)	–	–	–	–	159 (63)
	a	1	1	1	1	0.86 (0.04)
	molecules*	86.2 (4.7)	2.4 (1.1)	54.2 (1.2)	71.0 (3.7)	58.5 (3.7)
Si3	τ_1 (ps)	–	1477 (573)	28 (5)	21 (2)	24 (6)
	τ_2 (ps)	–	–	358 (101)	–	169 (39)
	a	–	–	0.70 (0.05)	1	0.65 (0.09)
	molecules*	–	95.4 (4.3)	4.4 (1.5)	3.5 (1.4)	8.3 (1.4)
NBO	τ_1 (ps)	–	144 (9)	17 (5)	19 (2)	20 (5)
	τ_2 (ps)	–	–	73 (36)	–	106 (35)
	a	–	–	0.72 (0.21)	1	0.70 (0.13)
	molecules*	–	1.9 (0.9)	14.1 (2.5)	6.0 (0.9)	15.9 (3.1)

The functions considered are of the form $N(t)/N_0 = a\exp\left(-t/\tau_1\right) + (1-a)\exp\left(-t/\tau_2\right)$, where N_0 is the number of molecules that are initially adsorbed, $N(t)$ the number of molecules that are still adsorbed at time t, τ_1 and τ_2 the mean adsorption times, and a the relative importance of τ_1. For the crystal pores (FullCr and PartCr) a simple exponential is fitted to the data ($a = 1$); whereas a double-exponential function is in general required for the amorphous pores (except for the MedAm and for the OH group in the LowAm, for which a single exponential is sufficient, $a = 1$). A single exponential is chosen if it is able to describe more than 90% of the population, we noticed that beyond this value the constants of the double-exponential fitting (τ_1, τ_2, a) are affected by severe uncertainty (the errors are higher than values themselves). The uncertainties on the fitted parameters, estimated as the standard deviation obtained from the covariance matrix, are given in parenthesis. The residence time of each molecule is calculated using the dominant-bond scheme with cutoff 5.5 Å for OH, and 4.5 Å for Si3 and NBO. * Number of CO_2 molecules initially found within the spherical regions defined by the cutoff distances, N_0, averaged over all initial frames. The uncertainty is estimated as the standard deviation.

Si3 sites: first, the majority of the Si3 are charge compensated by a vicinal NBO defect, reducing the Coulombic component of the bonding; second, most of the remaining Si3 have not been hydroxylated as they were not accessible to hydroxyl groups, indicating that they are less accessible also for bonding CO_2 molecules.

The mean adsorption times at the OH sites on the amorphous surfaces are reported in Table 3. The residence time (τ_1) is close to the residence time in the neighborhood of the OH groups that is observed in the FullCr (around 8 ps), suggesting that the distorted OH network of the amorphous pores has adsorption capacities comparable to the regular honeycomb structure of the FullCr.

In contrast to the FullCr (Figs. 6a), in the amorphous pores a fraction of the molecules remains adsorbed onto the OH longer than predicted by an exponential decay (Figs. 6b, 6c, and 6d). The fat tail in the adsorption-time distribution is caused by the variability of the bonds formed by the CO_2 molecules with the OH and its neighboring sites, and becomes more apparent when the number of defects increases (i.e., it is more pronounced in the LowAm than in MedAm, and even more in the HighAm). On the amorphous surfaces, each OH group is characterized by a different local arrangement of the surrounding atoms and the different inter-atomic distances vary the strength of the bonds formed between the surface and the CO_2 molecules. Moreover, the close presence of NBO and Si3 can also alter the adsorption onto the OH. However, as reported in the Methodology section, if the errors of the second time constants are higher than the mean values themselves, a single exponential is preferred to fit the data. This is the case in the LowAm and MedAm (Figs. 6c, and 6d) where the single exponential is able to describe the behavior of more than 90% of the adsorbed molecules. Only in the HighAm a double exponential is employed, with a second time constant (τ_2) representing 15 % of CO_2 molecules adsorbed at OH sites (Fig. 6b).

For the NBO and Si3 sites, the residence time of the CO_2 is considerably longer than for the OH sites. However, a significant variability is observed by comparing the high-density regions in Fig. 5. The strength of the interaction is determined by the specific local arrangement of the atoms and varies significantly across different sites. In the majority of cases (Fig. 5b, c), the high-density regions have very irregular shapes, which are caused by the interaction with the multiple sites that form nano-structures that adsorb CO_2 molecules for a longer time. Only in a few cases the CO_2 molecule interacts primarily with a single site, similarly to the PartCr (Fig. 5d).

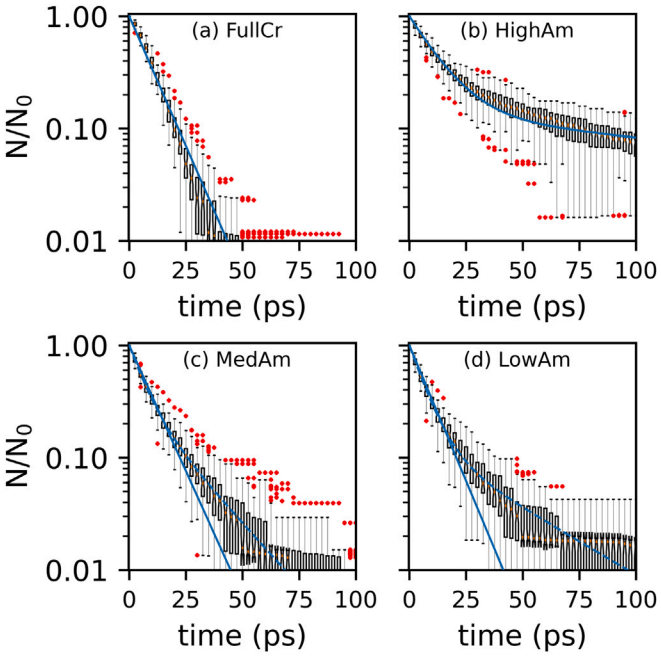

Fig. 6. Decay of CO_2 molecules, N_0, which are adsorbed onto an OH site on (a) the fully hydroxylated crystal pore (FullCr), (b) the high hydroxylation amorphous pore (HighAm), (c) the medium hydroxylation amorphous pore (MedAm), (d) the low hydroxylation amorphous pore (LowAm). The box plots represent the 0.25–0.5 quartiles (with whiskers extending for 1.5 times the inner quartile range), whereas the red dots are data outliers. The blue solid line is the fitted exponential (for the FullCr, LowAm, and MedAm) or double-exponential function (for HighAm) with parameters of Table 3. For the MedAm (c) and the LowAm (d) we also plot the double-exponential fitting (the dashed blue lines) to remark the minor differences between the two functions for the majority of the molecules (deviations are visible only in the tail for less than 10% of the molecules).

The heterogeneity in the strength of the bonds formed with Si3 and NBO requires a double exponential to describe the decaying time (except in the MedAm which has fewer defects than the other nanopores). The short-lived bonds are more likely and have mean adsorption time in the order of 20–30 ps for all surfaces and sites, whereas the long-lived bonds display a mean residence time that ranges from 70 up to

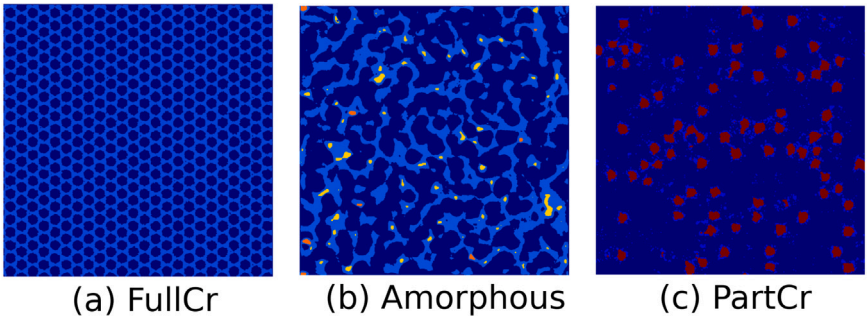

Fig. 7. Schematic illustrations of CO_2 adsorption features of silica surfaces: (a) On crystalline surfaces, the OH groups generate a regular and connected honeycomb structure characterized by intermediate density of CO_2 molecules (light blue); this feature dominates the adsorption onto the FullCr surface and provides a connected path for surface diffusion. (b) On the amorphous surfaces, the disorder leads to a distortion of the intermediate density region, which modifies the adsorption and surface-diffusion properties of the OH groups; in addition, the presence of coordination defects reinforces the adsorption of CO_2 leading to localized high-density (yellow) and very high-density regions in which short- and long-lived multiple bonds create cage-like structures (orange). (c) On the PartCr surface, the charge imbalance at Si3 defects surfaces creates regions of extremely high density (one order of magnitude higher than on amorphous surfaces) which dominate CO_2 adsorption (red); although locally distorted by the Si3 (and not visible here due to poor sampling), the connected honeycomb structure created by the OH groups is sill present and allows surface diffusion and hopping between Si3 defects (light blue).

400 ps. The residence times tend to be longer for Si3, even though these sites attract less CO_2 molecules in total. The long-lived bonds can be attributed to CO_2 molecules that remain trapped in the cage structures created by the local atomic arrangement in the surrounding of the defects.

Also the amorphous pores display a shorter mean adsorption time in the neighborhood of the individual sites, τ_1, which is sensibly shorter than the mean adsorption time in the surface layer. This indicates that the CO_2 molecules can diffuse from one individual site to another before desorbing from the surface layer.

4. Conclusions

To investigate the effects of disorder and the role played by surface defects, we simulated the adsorption of CO_2 in three prototypical amorphous nanopores, and compared the results with those obtained for crystalline surfaces. The MD simulations were performed with ClayFF, the force field that is currently employed to model the amorphous/CO_2 interface with good accuracy (see, e.g., [20,30,45]) and allowed us to investigate the impact of heterogeneity and coordination defects. It should be noticed, however, that the treatment of the charges on the defects should be improved if a more accurate quantitative description of adsorption onto amorphous surfaces is required. This can be done by means of computationally more expensive methods such as a charge equilibration scheme [64] that updates the charge repartition according to the coordination environment, a core–shell model that employs formal charges [65], or by devising machine-learning approaches that are trained to account for the variability induced by the amorphousness (to date, these approaches are only applicable to amorphous bulk systems [66,67]).

The MD simulations show that in fully hydroxylated crystals the CO_2 is adsorbed onto the connected honeycomb network formed by the regular periodic structure of the identical hydroxyl groups. The statistics of the adsorption-time is very well described by an exponential distribution. In contrast, the structural disorder of amorphous pores generates under-coordinated defects (in the form of three-fold coordinated silicon, Si3, and singly coordinated oxygen, NBO) and induces a non-negligible variability across the adsorption sites. Compared to a defect-free, fully hydroxylated crystalline surface, the rich variety of adsorption sites and bonds that can be formed with the CO_2 molecules enhances physisorption, yielding a much longer mean adsorption time and a residence-time distribution that is characterized by a fat tail.

The different surface features that characterize the adsorption on silica surfaces are depicted in Fig. 7. In the fully hydroxylated crystal, the molecules are adsorbed onto the honeycomb network in which they can diffuse from one OH group to the other, undergoing multiple adsorption events before desorption (Fig. 7a). On defected crystal surfaces, which are characterized by charged coordination defects in the form of Si3 and NBO (PartCr), the local oxygen vacancies at the Si3 sites dominate the adsorption and lead to extremely long residence times of the CO_2 molecules in isolated circular adsorption sites (Fig. 7c). In the amorphous pores most CO_2 adsorbs onto the network formed by the hydroxyl groups, which is distorted by the underlying amorphous surfaces (Fig. 7b). This network, reminiscent of the honeycomb structure of the fully hydroxylated crystal, allows for surface diffusion between regions of higher CO_2 density that are embedded into the network. These regions are located in correspondence of under-coordinated defects that affect the local structure of the amorphous surface and can promote the formation of cage-like structures in which the CO_2 molecules can remain trapped by forming multiple bonds with the surrounding atoms.

The complexity and the variability of the features encountered on the amorphous surfaces enhance physisorption by allowing for longer-lived bonds induced by under-coordination defects. As physisorption of the reactant molecules is necessary to initiate heterogeneous catalysis, our findings support the recent experimental discovery that defected silica surfaces can fix and catalytically convert CO_2 into methane [2,68,69]. By appropriate design and manufacturing it may be possible to optimize the adsorption regions for specific catalytic reactions. This will require the development of new methods that are specifically designed for amorphous surfaces and can help us to better analyze and classify their irregular adsorption features. We envisage that machine-learning algorithms can be used to segment the amorphous surface according to the adsorption capacity and to correlate the high-density regions to the underneath amorphous structure, revealing the details of the mechanisms that enhance adsorption and helping the design of heterogeneous catalysts.

CRediT authorship contribution statement

Mattia Turchi: Conceptualization of the overall study, simulations, analysis and visualization of the data, writing – original draft, critical review and editing of the manuscript. **Sandra Galmarini:** Conceptualization of the overall study, analysis of the results, writing – critical review and editing of the manuscript. **Ivan Lunati:** Conceptualization of the overall study, analysis of the results, supervision, writing – critical review and editing of the manuscript.

Declaration of competing interest

The authors declare that they have no known competing financial interests or personal relationships that could have appeared to influence the work reported in this paper.

Data availability

Data will be made available on request.

Acknowledgments

We acknowledge support of the Empa Internal Research Call (IRC 2021) under the project "Multiscale modeling of carbon dioxide adsorption in functionalized silica aerogels". The simulation were performed on Piz Daint at the Swiss National Supercomputing Centre (Centro Svizzero di Calcolo Scientifico, Manno, Switzerland) under Empa's share with project ID em13. We thank Tran Thi Bao Le and Alberto Striolo for sharing the structure of the β-cristobalite surface which we was used in our work.

Appendix A. Supplementary data

Supplementary material related to this article can be found online at https://doi.org/10.1016/j.jnoncrysol.2023.122709.

References

[1] M.Y.S. Hamid, M.L. Firmansyah, S. Triwahyono, A.A. Jalil, R.R. Mukti, E. Febriyanti, V. Suendo, H.D. Setiabudi, M. Mohamed, W. Nabgan, Oxygen vacancy-rich mesoporous silica KCC-1 for CO2 methanation, Appl. Catal. A Gen. 532 (2017) 86–94.

[2] Amit K. Mishra, Rajesh Belgamwar, Rajkumar Jana, Ayan Datta, Vivek Polshettiwar, Defects in nanosilica catalytically convert CO2 to methane without any metal and ligand, Proc. Natl. Acad. Sci. 117 (12) (2020) 6383–6390.

[3] Linards Skuja, Nadège Ollier, Koichi Kajihara, Krisjanis Smits, Creation of glass-characteristic point defects in crystalline SiO2 by 2.5 MeV electrons and by fast neutrons, J. Non-Cryst. Solids 505 (2019) 252–259.

[4] P.V. Sushko, S. Mukhopadhyay, A.M. Stoneham, A.L. Shluger, Oxygen vacancies in amorphous silica: structure and distribution of properties, Microelectron. Eng. 80 (2005) 292–295.

[5] C.J. Brinker, R.J. Kirkpatrick, D.R. Tallant, B.C. Bunker, B. Montez, NMR confirmation of strained "defects" in amorphous silica, J. Non-Cryst. Solids 99 (2–3) (1988) 418–428.

[6] Albert Rimola, Dominique Costa, Mariona Sodupe, Jean-Francois Lambert, Piero Ugliengo, Silica surface features and their role in the adsorption of biomolecules: computational modeling and experiments, Chem. Rev. 113 (6) (2013) 4216–4313.

[7] Jonas G. Croissant, Kimberly S. Butler, Jeffrey I. Zink, C. Jeffrey Brinker, Synthetic amorphous silica nanoparticles: toxicity, biomedical and environmental implications, Nat. Rev. Mater. 5 (12) (2020) 886–909.

[8] Haiyuan Zhang, Darren R. Dunphy, Xingmao Jiang, Huan Meng, Bingbing Sun, Derrick Tarn, Min Xue, Xiang Wang, Sijie Lin, Zhaoxia Ji, et al., Processing pathway dependence of amorphous silica nanoparticle toxicity: colloidal vs pyrolytic, J. Am. Chem. Soc. 134 (38) (2012) 15790–15804.

[9] I.A. Rahman, P. Vejayakumaran, C.S. Sipaut, J. Ismail, C.K. Chee, Size-dependent physicochemical and optical properties of silica nanoparticles, Mater. Chem. Phys. 114 (1) (2009) 328–332.

[10] Linards Skuja, Optically active oxygen-deficiency-related centers in amorphous silicon dioxide, J. Non-Cryst. Solids 239 (1) (1998) 16–48.

[11] Daniel F. Shantz, Jörn Schmedt auf der Günne, Hubert Koller, Raul F. Lobo, Multiple-quantum 1H MAS NMR studies of defect sites in as-made all-silica ZSM-12 zeolite, J. Am. Chem. Soc. 122 (28) (2000) 6659–6663.

[12] Al-Moatasem El-Sayed, Matthew B. Watkins, Tibor Grasser, Valery V. Afanas'ev, Alexander L. Shluger, Hydrogen-induced rupture of strained Si-O bonds in amorphous silicon dioxide, Phys. Rev. Lett. 114 (2015) 115503.

[13] Frederik Tielens, Maciej Gierada, Jarosław Handzlik, Monica Calatayud, Characterization of amorphous silica based catalysts using DFT computational methods, Catal. Today 354 (2020) 3–18, SI: Fascinating catalysis.

[14] Maciej Gierada, Frank De Proft, Marialore Sulpizi, Frederik Tielens, Understanding the acidic properties of the amorphous hydroxylated silica surface, J. Phys. Chem. C 123 (28) (2019) 17343–17352.

[15] Livia Giordano, Peter V. Sushko, Gianfranco Pacchioni, Alexander L. Shluger, Electron trapping at point defects on hydroxylated silica surfaces, Phys. Rev. Lett. 99 (2007) 136801.

[16] Anant D. Kulkarni, Donald G. Truhlar, Sriram Goverapet Srinivasan, Adri C.T. van Duin, Paul Norman, Thomas E. Schwartzentruber, Oxygen interactions with silica surfaces: Coupled cluster and density functional investigation and the development of a new ReaxFF potential, J. Phys. Chem. C 117 (1) (2013) 258–269.

[17] Joseph C. Fogarty, Hasan Metin Aktulga, Ananth Y. Grama, Adri C.T. van Duin, Sagar A. Pandit, A reactive molecular dynamics simulation of the silica- water interface, J. Chem. Phys. 132 (17) (2010) 174704.

[18] Ali A. Hassanali, Sherwin J. Singer, Model for the water-amorphous silica interface: The undissociated surface, J. Phys. Chem. B 111 (38) (2007) 11181–11193, PMID: 17803296.

[19] Tran Thi Bao Le, Alberto Striolo, David R. Cole, Partial CO2 reduction in amorphous cylindrical silica nanopores studied with reactive molecular dynamics simulations, J. Phys. Chem. C 123 (43) (2019) 26358–26369.

[20] Xiaoning Yang, Zhijun Xu, Cuijuan Zhang, Molecular dynamics simulation of dense carbon dioxide fluid on amorphous silica surfaces, J. Colloid Interface Sci. 297 (1) (2006) 38–44.

[21] J.M. Rimsza, R.E. Jones, L.J. Criscenti, Surface structure and stability of partially hydroxylated silica surfaces, Langmuir 33 (15) (2017) 3882–3891.

[22] Tiffany R. Walsh, Mark Wilson, Adrian P. Sutton, Hydrolysis of the amorphous silica surface. II. Calculation of activation barriers and mechanisms, J. Chem. Phys. 113 (20) (2000) 9191–9201.

[23] Fei Wang, Shan He, Hao Chen, Bin Wang, Lirong Zheng, Min Wei, David G. Evans, Xue Duan, Active site dependent reaction mechanism over Ru/CeO2 catalyst toward CO2 methanation, J. Am. Chem. Soc. 138 (19) (2016) 6298–6305, PMID: 27135417.

[24] Lin Tao, Davoud Dastan, Wensen Wang, Preeyaporn Poldorn, Xianze Meng, Mingjie Wu, Hongwei Zhao, Han Zhang, Lixiang Li, Baigang An, Metal-decorated InN monolayer senses N2 against CO2, ACS Appl. Mater. Interfaces 15 (9) (2023) 12534–12544.

[25] Umberto Martinez, Gianfranco Pacchioni, Interaction of CO, CO2 and CH4 with mesoporous organosilica: Periodic DFT calculations with dispersion corrections, Microporous Mesoporous Mater. 129 (1) (2010) 62–67.

[26] Sakiru B. Badmos, Alberto Striolo, David R. Cole, Aqueous hydrogen sulfide in slit-shaped silica nanopores: Confinement effects on solubility, structural, and dynamical properties, J. Phys. Chem. C 122 (26) (2018) 14744–14755, Publisher: American Chemical Society.

[27] Siddharth Gautam, Thu Le, Alberto Striolo, David Cole, Molecular dynamics simulations of propane in slit shaped silica nano-pores: direct comparison with quasielastic neutron scattering experiments, Phys. Chem. Chem. Phys. 19 (48) (2017) 32320–32332, Publisher: The Royal Society of Chemistry.

[28] Dimitrios Argyris, Naga Rajesh Tummala, Alberto Striolo, David R. Cole, Molecular structure and dynamics in thin water films at the silica and graphite surfaces, J. Phys. Chem. C 112 (35) (2008) 13587–13599, Publisher: American Chemical Society.

[29] Thu Le, Alberto Striolo, David R. Cole, CO2–C4H10 mixtures simulated in silica slit pores: Relation between structure and dynamics, J. Phys. Chem. C 119 (27) (2015) 15274–15284, Publisher: American Chemical Society.

[30] Sabine Leroch, Martin Wendland, Simulation of forces between humid amorphous silica surfaces: A comparison of empirical atomistic force fields, J. Phys. Chem. C 116 (50) (2012) 26247–26261.

[31] Pubudu N. Wimalasiri, Nuong P. Nguyen, Hasini S. Senanayake, Brian B. Laird, Ward H. Thompson, Amorphous silica slab models with variable surface roughness and silanol density for use in simulations of dynamics and catalysis, J. Phys. Chem. C 125 (42) (2021) 23418–23434.

[32] M. Turchi, Sheersha Perera, S. Ramsheh, A.J. Popel, D.V. Okhrimenko, S.L.S. Stipp, M. Solvang, M.P. Andersson, T.R. Walsh, Predicted structures of calcium aluminosilicate glass as a model for stone wool fiber: effects of composition and interatomic potential, J. Non-Cryst. Solids 567 (2021) 120924.

[33] S. Miri Ramsheh, M. Turchi, S. Perera, A.M. Schade, D.V. Okhrimenko, S.L.S. Stipp, M. Solvang, T.R. Walsh, M.P. Andersson, Prediction of the surface chemistry of calcium aluminosilicate glasses, J. Non-Cryst. Solids 620 (2023) 122597.

[34] F. Vuković, N.A. Garcia, S. Perera, M. Turchi, M.P. Andersson, M. Solvang, P. Raiteri, T.R. Walsh, Atomistic simulations of calcium aluminosilicate interfaced with liquid water, J. Chem. Phys. 159 (10) (2023).

[35] Randall T. Cygan, Jian-Jie Liang, Andrey G. Kalinichev, Molecular models of hydroxide, oxyhydroxide, and clay phases and the development of a general force field, J. Phys. Chem. B 108 (4) (2004) 1255–1266, Publisher: American Chemical Society.

[36] Tuan A. Ho, D. Argyris, D.R. Cole, A. Striolo, Aqueous NaCl and CsCl solutions confined in crystalline slit-shaped silica nanopores of varying degree of protonation, Langmuir 28 (2) (2012) 1256–1266, Publisher: American Chemical Society.

[37] Steve Plimpton, Fast parallel algorithms for short-range molecular dynamics, J. Comput. Phys. 117 (1) (1995) 1–19.

[38] Jincheng Du, Alastair N. Cormack, Molecular dynamics simulation of the structure and hydroxylation of silica glass surfaces, J. Am. Ceram. Soc. 88 (9) (2005) 2532–2539, Publisher: John Wiley & Sons, Ltd.

[39] J. Lane, Matthew D., Cooling rate and stress relaxation in silica melts and glasses via microsecond molecular dynamics, Phys. Rev. E 92 (2015) 012320.

[40] J. Du, A.N. Cormack, The medium range structure of sodium silicate glasses: a molecular dynamics simulation, in: Glass Science for High Technology. 16th University Conference on Glass Science, Vol. 349, 2004, pp. 66–79.

[41] Randall T. Cygan, Vyacheslav N. Romanov, Evgeniy M. Myshakin, Molecular simulation of carbon dioxide capture by montmorillonite using an accurate and flexible force field, J. Phys. Chem. C 116 (24) (2012) 13079–13091.
[42] Jonathan G. Harris, Kwong H. Yung, Carbon dioxide's liquid-vapor coexistence curve and critical properties as predicted by a simple molecular model, J. Phys. Chem. 99 (31) (1995) 12021–12024, Publisher: American Chemical Society.
[43] Jennifer C. Crabtree, Marco Molinari, Stephen C. Parker, John A. Purton, Simulation of the adsorption and transport of CO2 on faujasite surfaces, J. Phys. Chem. C 117 (42) (2013) 21778–21787, Publisher: American Chemical Society.
[44] J.A. Purton, Jenny C. Crabtree, S.C. Parker, DL_MONTE: a general purpose program for parallel Monte Carlo simulation, Mol. Simul. 39 (14–15) (2013) 1240–1252.
[45] Ian C. Bourg, Carl I. Steefel, Molecular dynamics simulations of water structure and diffusion in silica nanopores, J. Phys. Chem. C 116 (21) (2012) 11556–11564, Publisher: American Chemical Society.
[46] Hideo Ohno, Shinji Kohara, Norimasa Umesaki, Kentaro Suzuya, High-energy X-ray diffraction studies of non-crystalline materials, J. Non-Cryst. Solids 293 (2001) 125–135.
[47] Pierre Hudon, In-Ho Jung, Don R. Baker, Melting of β-quartz up to 2.0 GPa and thermodynamic optimization of the silica liquidus up to 6.0 GPa, Phys. Earth Planet. Inter. 130 (3–4) (2002) 159–174.
[48] Takashi Takei, Atsushi Yamazaki, Tohru Watanabe, Masatoshi Chikazawa, Water adsorption properties on porous silica glass surface modified by trimethylsilyl groups, J. Colloid Interface Sci. 188 (2) (1997) 409–414.
[49] Joël Puibasset, Roland J.-M. Pellenq, Grand canonical Monte Carlo simulation study of water structure on hydrophilic mesoporous and plane silica substrates, J. Chem. Phys. 119 (17) (2003) 9226–9232, Publisher: American Institute of Physics.
[50] Thu Le, Alberto Striolo, David R. Cole, Propane simulated in silica pores: Adsorption isotherms, molecular structure, and mobility, in: 2013 Danckwerts Special Issue on Molecular Modelling in Chemical Engineering, Vol. 121, 2015, pp. 292–299.
[51] L.T. Zhuravlev, The surface chemistry of amorphous silica. Zhuravlev model, Colloids Surf. A 173 (1) (2000) 1–38.
[52] Donald B. Peacor, High-temperature single-crystal study of the cristobalite inversion, Z. Kristallogr. (Cryst. Mater.) 138 (1–6) (1973) 274–298.
[53] Lester Guttman, Ring structure of the crystalline and amorphous forms of silicon dioxide, J. Non-Cryst. Solids (Netherlands) 116 (1990).
[54] B.P. Feuston, S.H. Garofalini, Oligomerization in silica sols, J. Phys. Chem. 94 (13) (1990) 5351–5356, Publisher: American Chemical Society.
[55] Shūichi Nosé, A molecular dynamics method for simulations in the canonical ensemble, Mol. Phys. 52 (2) (1984) 255–268.
[56] William G. Hoover, Canonical dynamics: Equilibrium phase-space distributions, Phys. Rev. A 31 (1985) 1695–1697.
[57] Roger W. Hockney, James W. Eastwood, Computer Simulation using Particles, crc Press, 2021.
[58] David S. Cerutti, Robert E. Duke, Thomas A. Darden, Terry P. Lybrand, Staggered mesh ewald: An extension of the smooth particle-mesh ewald method adding great versatility, J. Chem. Theory Comput. 5 (9) (2009) 2322–2338.
[59] Alexey Neelov, Christian Holm, Interlaced P3M algorithm with analytical and ik-differentiation, J. Chem. Phys. 132 (23) (2010) 234103.
[60] L.T. Zhuravlev, Concentration of hydroxyl groups on the surface of amorphous silicas, Langmuir 3 (3) (1987) 316–318.
[61] T. Tepper, S. Berger, Correlation between microstructure, particle size, dielectric constant, and electrical resistivity of nano-size amorphous SiO2 powder, Nanostruct. Mater. 11 (8) (1999) 1081–1089.
[62] Lin Tao, Junchen Huang, Davoud Dastan, Tianyu Wang, Jing Li, Xitao Yin, Qi Wang, New insight into absorption characteristics of CO2 on the surface of calcite, dolomite, and magnesite, Appl. Surf. Science 540 (2021) 148320.
[63] Tran Thi Bao Le, Alberto Striolo, David R. Cole, Partial CO2 reduction in amorphous cylindrical silica nanopores studied with reactive molecular dynamics simulations, J. Phys. Chem. C 123 (43) (2019) 26358–26369, Publisher: American Chemical Society.
[64] Sebastian Spicher, Stefan Grimme, Robust atomistic modeling of materials, organometallic, and biochemical systems, Angew. Chem., Int. Ed. 59 (36) (2020) 15665–15673.
[65] Nora H. de Leeuw, F. Manon Higgins, Stephen C. Parker, Modeling the surface structure and stability of α-quartz, J. Phys. Chem. B 103 (8) (1999) 1270–1277.
[66] Linus C Erhard, Jochen Rohrer, Karsten Albe, Volker L Deringer, A machine-learned interatomic potential for silica and its relation to empirical models, npj Comput. Mater. 8 (1) (2022) 90.
[67] Albert P. Bartók, James Kermode, Noam Bernstein, Gábor Csányi, Machine learning a general-purpose interatomic potential for silicon, Phys. Rev. X 8 (4) (2018) 041048.
[68] Lingxiang Wang, Erjia Guan, Yeqing Wang, Liang Wang, Zhongmiao Gong, Yi Cui, Xiangju Meng, Bruce C Gates, Feng-Shou Xiao, Silica accelerates the selective hydrogenation of CO2 to methanol on cobalt catalysts, Nat. Commun. 11 (1) (2020) 1033.
[69] Vivek Polshettiwar, Dendritic fibrous nanosilica: discovery, synthesis, formation mechanism, catalysis, and co2 capture–conversion, Acc. Chem. Res. 55 (10) (2022) 1395–1410.